Journal of Photochemistry & Photobiology, A: Chemistry 467 (2025) 116454

Contents lists available at ScienceDirect

Journal of Photochemistry & Photobiology, A: Chemistry

journal homepage: www.elsevier.com/locate/jphotochem

A novel N-doped porous carbon-supported g-C_3N_4 composite for enhanced photocatalytic CO_2 conversion

Roopesh Mekkat [a,*], Edith Mawunya Kutorglo [a], Milena Setka [a], Andrey. Prokhorov [b,c], Miroslav Šoóš [a,*]

[a] University of Chemistry and Technology, Department of Chemical Engineering, Technická 3, Prague 160 00, Czech Republic
[b] Institute of Physics AS CR, Na Slovance 2, Prague 18221, Czech Republic
[c] Institute of Plasma Physics of the Czech Academy of Sciences, Prague 182 00, Czech Republic

ARTICLE INFO

Keywords:
g-C_3N_4
Porous carbon
CO_2 capture
Photocatalysis
CO_2 reduction

ABSTRACT

The solar light-driven CO_2 conversion into hydrocarbon fuels is regarded as one of the most crucial inventions to reduce CO_2 abundance in the atmosphere and fulfill energy needs. Graphitic carbon nitride (g-C_3N_4) has garnered considerable attention and emerges as a promising candidate for photocatalytic CO_2 reduction, owing to its visible light absorption, metal-free, and environmentally benign nature. However, its ability to effectively achieve this is currently hindered by several factors such as relatively low surface area, fast electron-hole recombination rate and limited CO_2 adsorption capacity, which also constrain its practical applicability. In this work, a novel photocatalyst was synthesized by incorporating a suitable amount of ZIF-8 derived N-doped porous carbon into g-C_3N_4 without affecting its light absorption capacity. The as-prepared samples were characterized by X-ray diffraction (XRD), transmission electron microscopy (TEM), Fourier transform infrared spectroscopy (FT-IR), nitrogen and CO_2 adsorption measurements, X-ray photoelectron spectroscopy (XPS), UV–Vis diffuse reflectance absorption spectra (UV-DRS), and photoluminescence spectroscopy (PL). Compared to g-C_3N_4, the optimized photocatalyst exhibited a 54-fold increase in surface area, a 3.5-fold enhancement in CO_2 adsorption capacity, a reduced optical bandgap, and significantly superior photocatalytic activity for CO_2 reduction, achieving CH_4 production at 70.87 μmol h^{-1} g^{-1} and C_2H_6 production at 35.31 μmol h^{-1} g^{-1}. The enhanced activity of the composites is attributed to the synergistic effect of the N-doped carbon and g-C_3N_4. Thus, this approach offers a promising strategy for the future development of C_3N_4-based catalysts for efficient solar to fuel conversion.

1. Introduction

Demand for energy is increasing day by day due to worldwide economic growth and overall industrial development. According to the International Energy Agency (IEA) report 2022, global Total Primary Energy Supply (TPES) has almost doubled, and 80 % of TPES is sourced from fossil fuels, resulting in persistently high levels of greenhouse gas (GHG) emissions [1]. The new policy of IEA, that is the Net Zero Emissions by 2050 (NZE) scenario, maps out a way to achieve a 1.5 °C stabilization in the rise in global average temperatures, alongside universal access to modern energy by 2030. Therefore, the conversion of CO_2 into fuels or hydrocarbons and utilizing the abundantly available solar energy are effective strategies that can provide a solution to the two key societal challenges, i.e., meeting energy demand and mitigating the greenhouse gas effect. Besides, exploring the scope for the utilization of CO_2 as an alternative low-cost renewable energy source is also a stimulating sector [2–8]. Generally, carbon capture and storage require a high amount of energy and cost. Therefore, it would be worth the effort to synthesize materials that can simultaneously adsorb and convert CO_2 into useful products like hydrocarbon fuels. This innovation can diminish our reliance on fossil fuels and will be able to regulate the emission of GHGs, hence controlling global warming. To address the increasing levels of carbon dioxide (CO_2) in the atmosphere and find solutions to mitigate the rise, researchers are exploring the potential of new materials. One interesting approach is to develop materials that combine properties to tackle multiple challenges at once, the so-called multifunctional materials. Thus, the utilization of photocatalysis for the reduction of CO_2 and to generate hydrocarbon fuels, presents an

* Corresponding authors.
E-mail addresses: mekkatr@vscht.cz (R. Mekkat), miroslav.soos@vscht.cz (M. Šoóš).

https://doi.org/10.1016/j.jphotochem.2025.116454
Received 5 January 2025; Received in revised form 27 March 2025; Accepted 21 April 2025
Available online 22 April 2025

appealing solution to tackle two pressing challenges simultaneously: the overdependence on fossil fuels and environmental pollution [9–12].

Semiconductor photocatalytic technology has the characteristics of low-cost, energy-saving and high efficiency, having been deeply studied and widely used in the photocatalytic reduction of CO_2 [13,14]. Most of the developed photocatalysts are metal-containing materials, which makes them costly for large-scale applications and can lead to environmental pollution due to metal ion leaching. Hence, researchers are investigating metal-free photocatalysts with reasonable activity for CO_2 reduction [15,16]. Among all the non-metal semiconductors, graphitic carbon nitride (g-C_3N_4) is one of the most promising and intensively studied photocatalysts due to its advantageous properties such as low cost, facile synthesis, good stability, relatively narrow band gap and excellent photocatalytic performance with good visible light response [17–20]. However, the investigation into the reduction of CO_2 using composite materials made of g-C_3N_4 is still in its nascent stages. Furthermore, the product yield for the photoreduction of CO_2 remains minimal in most reports. This is mainly because pristine g-C_3N_4 normally displays limited CO_2 photocatalytic reduction performance due to the insufficient carbon–nitrogen ratio, dense surface defects, narrow spectral response, relatively low surface area, fast electron-hole recombination rate, low CO_2 adsorption capacity, and limited active sites [21,22]. Several endeavors have been dedicated to addressing these drawbacks like doping with metal/non-metal, constructing heterojunctions, synthesis of g-C_3N_4 composites with specific morphology and surface function, etc. Among them, customization of g-C_3N_4 through surface modifications has emerged as a novel approach for enhancing photocatalytic performance [23–27].

Nowadays, carbons with porous structures in the nano-dimensions are becoming good competitors to Metal Organic Framework (MOF), Covalent Organic Framework (COF), and zeolites in the area of CO_2 capture. They are becoming superior candidates for enhanced adsorption of CO_2 molecules on the surface of photocatalysts to facilitate their catalytic conversion. The overall advantages including inexpensive precursors, simple preparation methods, unique textural and physicochemical properties make them potential candidates for CO_2 capture [28–30]. In addition, earlier studies confirm that the nitrogen-containing functional groups can further enhance CO_2 uptake through electrostatic, Lewis acid-base, and hydrogen-bonding interactions [31–34]. Nonetheless, the potential of utilizing the CO_2 capturing capabilities of these porous carbons in the area of photocatalytic CO_2 reduction remains largely unexplored.

Herein, we developed a metal-free photocatalyst that can perform efficient CO_2 reduction and attain a remarkable CO_2 adsorption capacity with enhanced surface area. The photocatalytically active g-C_3N_4 material was synthesized from melamine via simple polymerization at 550 ^{0}C for 3 h. The surface of g-C_3N_4 was then modified by N-doped hierarchically porous carbon synthesized via pyrolysis of ZIF-8, which has a high surface area and abundant adsorption sites for CO_2 adsorption. Loading different weight percentages of porous N-doped carbon into g-C_3N_4 resulted in an optimized composite, which exhibited superior activity for the photocatalytic reduction of CO_2 into valuable hydrocarbon products, such as methane (CH_4) and ethane (C_2H_6), with excellent conversion efficiency.

2. Experimental section

2.1. Materials

Melamine (> 99 %), Zinc nitrate hexahydrate p.a. (≥ 99 %), 2-Methylimidazole (99 %), Sodium sulfate, and Ethanol were purchased from Sigma Aldrich. Hydrochloric acid (35 % G.R.), Potassium hydroxide, Methanol p.a. (≥ 99 %), were purchased from Lach-Ner, Ltd. All chemicals were used without further purification. Ultra-pure water was used throughout all experiments.

2.2. Synthesis of g-C_3N_4 sheets

Melamine was used as precursor for the synthesis of g-C_3N_4 semiconductor via a simple poly-condensation reaction [35,36]. First, 10 g of melamine was placed in a closed crucible and heated to 550 °C at a heating rate of 10 °C min^{-1} for 3 h in air. After 3 h, the oven is switched off and the material was left in the furnace to cool down to room temperature. The yellow product g-C_3N_4 was collected and ground into powder and labelled as CN.

2.3. Synthesis of N-doped porous carbon

ZIF-8 was synthesized by a simple wet chemical method [37]. About 11.88 g (0.04 mol) of zinc nitrate hexahydrate ($Zn(NO_3)_2$. 6 H_2O) was dissolved in 200 mL of methanol. Then, 19.68 g (0.24 mol) of 2-methylimidazole (2-Me-Im) was dissolved in 200 mL of methanol and slowly added to the above solution using a programmable syringe pump at a rate of 23 mL/min. The reaction was carried out for 24 h at room temperature under stirring (200 rpm). The resulting white suspension was washed several times by centrifugation in methanol (12000 rpm, 25 min). The resulting white powder was dried at 80 °C in the air.

The N-doped porous carbons were obtained by thermal treatment in a tube furnace, under nitrogen atmosphere with a flow rate of 50 L/h. The synthesized ZIF-8 sample was placed in a combustion ceramic dish and heated to 200 °C at a rate of 15 °C/min. The sample was held at this temperature for 30 min to get rid of any residual solvent and water vapor. The temperature was then increased to the target carbonization temperature, 800 °C, at the same heating rate and carbonized for 4 h. The oven was switched off and the material was allowed to cool down naturally to room temperature under nitrogen atmosphere. The carbonization product was washed using 1 M HCl (sonicated for 10 min) to remove residual Zn component. Then, the sample was rinsed with deionized (DI) water until neutral and dried overnight under vacuum at 65 °C. The as-synthesized porous carbon materials were chemically activated to create additional hierarchical porosity in the material by mixing with KOH flakes (mass ratio 2:1, m_{KOH}: m_{ZIF8}) in dry form, then 25 mL of DI water was added, and the mixture was sonicated in an ultrasonic bath for 60 min. Subsequently, the mixture was placed onto a hot plate and left to evaporate completely. The dried mixture was transferred into a combustion ceramic dish and followed the same carbonization procedure as described above. The as-treated black powder sample was denoted as NCZ.

2.4. Synthesis of NCZ(x%)CNy composite

Calculated amounts of CN and NCZ were dispersed in water separately, and the two dispersions were mixed with each other. The mixture was stirred for 1 h (150 rpm) at room temperature and then dried on a hotplate at 80 ^{0}C. The dried sample was annealed at 300 ^{0}C for 2 h in a muffle furnace at the rate of 5 °C/min in air, and a grey-coloured powder was obtained. Various amounts of NCZ were loaded onto the CN structure. The reaction was carried out at pH 4.5, which was optimized by zeta potential studies. To adjust the pH, 0.1 M HCl solution was used. In order to study the effect of pH on synthesis, the reaction was also carried out without any pH adjustment (pH ~ 7). The product was denoted as NCZ(x%)CNy (where x = weight percentage of NCZ loading, i.e., 3 %, 5 %, and 7%, y = pH of the dispersions during synthesis).

2.5. Characterization

The prepared products were characterized using different analytical techniques. The crystal phases of the as-prepared materials were analyzed by powder X-ray diffraction (XRD) with an X'Pert3 Powder diffractometer (*Malvern Panalytical*, United Kingdom) using CuKα radiation (λ = 1.5418 Å, U = 40 kV, I = 30 mA) over a 2θ range of 5–80° with a step size of 0.04°. Fourier transform infrared (FTIR) spectra were

recorded on FT-IR spectrometer Nicolet 6700 (*Thermo Fisher Scientific*, US), with samples dispersed in KBr pellets using 64 scans and a resolution of 4 cm^{-1}. The zeta potential measurements of the samples were performed on a Malvern, Zetasizer Nano, ZS90 at room temperature. Before the measurements, 5 mg of each powder sample was well ground and dispersed in deionized water (100 mL) by ultrasonication for 15 min, followed by vacuum filtration using 5 μm filter paper. The zeta potential was measured at different pH values. Scanning electron microscope (SEM) of Vega 3 (*Tescan*, Czechia) together with transmission electron microscopy (TEM) of EFTEM 2200 FS (*Jeol, Japan)* electron microscope, equipped with 200 kV field emission gun (electron source: ZrO/W Schottky emitter) and in-column energy (Omega) filter, were used to examine the morphology of the as-prepared samples.

Thermogravimetric Analysis (TGA) studies were performed on a Setaram Labsys EVO device. Approximately 10 mg of catalyst was deposited in an alumina crucible that was inserted into the system. The sample was heated from ambient temperature to 800 °C (heating ramp 5 °C/min) using an airflow of 50 mL/min. The Brunauer-Emmett-Teller (BET) specific surface area was calculated from a multipoint BET method, and CO_2 adsorption capacities were determined using the device Quantachrome Nova 2200e (Anton-Paar, AUT). All the samples were degassed at 150 °C for 6 h before the adsorption measurements. The surface chemistry of the samples was analyzed with X-ray photoelectron spectroscopy (XPS) (Kratos Axis Supra, Manchester, UK) with monochromatic Al Kα X-ray radiation. A pass energy of 80 eV and 20 eV, respectively, was used to measure the wide and narrow spectra. All the binding energies were calibrated using the C 1 s peak at 284.8 eV. The EPR spectra were measured at X-band (9.384 GHz) using the Bruker E580 ELEXSYS spectrometer equipped with the ER 4122 SHQE Super X High-Q cavity. The samples were placed in quartz tubes with a diameter of 4 mm. The following experimental parameters were used for the EPR measurements: microwave power of 1.5 mW, modulation frequency of 100 kHz, modulation amplitude of 0.5 mT, and a conversion time of 60 ms (number of scans: 4). The measurements were performed at room temperature (T = 295 K).

The photoluminescence spectra were measured with a fluorescence spectrophotometer (RAMANLOG 6, USA) using 256 nm lasers as the excitation source. The optical properties were analyzed by diffuse reflectance spectroscopy (DRS) on an Agilent Cary 60 UV–vis spectrophotometer, with $BaSO_4$ as the reflectance standard. The band gap of the prepared catalysts were estimated from the tauc equation using the Kubelka-Munk function [38].

$$(\alpha h\nu)^{1/2} = A(h\nu - Eg) \quad (1)$$

Where α, hν, Eg, and A were absorption coefficient, the photon energy, bandgap and a constant, respectively.

The data were plotted and analyzed using Origin 2019b Pro software package.

2.6. Electrochemical measurements

To evaluate the conductivity and resistance of the materials under investigation, a standard three-electrode setup was employed. The linear sweep voltammetry (LSV) test was conducted using a 0.5 M Na_2SO_4 electrolyte solution with a scan rate of 10 mV/s. Counter and reference electrodes were made of Pt and Ag/AgCl in a saturated KCl solution, respectively. The working electrodes were prepared as follows: 10 mg of the synthesized sample was mixed with 1 mL of DI water and sonicated to achieve a homogeneous blend. The resulting homogeneous ink was then pipetted onto a polished glassy carbon electrode and then dried at room temperature. Then 2 μl of 5 wt% Nafion in ethanol solution was dried on catalyst modified glassy carbon electrode. Electrochemical impedance spectroscopy (EIS) was performed at a bias potential of 0.2 V. Data collection and processing were carried out using Thermo Scientific OMNIC 8.0 software (ThermoFisher Scientific, Waltham, MA, USA). The data were plotted and analyzed using Origin 2019b Pro.

2.7. Photocatalytic CO_2 reduction tests

The CO_2 reduction performance of the synthesized photocatalysts was tested in a 100 mL glass photoreactor with a top irradiation window fitted with quartz glass (Fig. S1). All experiments were run under simulated solar light conditions, and triethanolamine (TEA) was used as a renewable sacrificial agent. In a typical experiment, 10 mg of the photocatalyst was placed into the reactor, and 20 mL of 10 vol% TEA solution was added. After closing the reactor with a septum fitted cap, the reactor was connected to a Schlenk line and purged with carbon dioxide for 30 – 45 min to replace the air in the headspace with carbon dioxide. Using a solar simulator equipped with an AM 1.5 filter (from L. O.T. Oriel Quantum Design, Germany), the reaction mixture was then irradiated under constant stirring for 3 – 7 h, depending on the experimental parameters under consideration. The products formed at the end of the reaction were analysed by gas chromatography. For the chromatographic analysis, 10 mL of gas sample was collected from the headspace using an airtight syringe that had been pre-cleaned with argon twice. Two samples of 5 mL each were manually injected into the gas chromatograph (GC Agilent 7890 A) equipped with a Flame Ionization Detector (FID), a thermal conductivity detector (TCD), and a methanizer. The amount of products in mmol was calculated as follows using the molar volume V_m (gas) of the detected gas at 25 °C = 24.5 L mol^{-1} and $V_{Headspace}$, the headspace volume = 80 mL.

$$\text{Gas produced} = \frac{\text{Gas (detected by the GC)}}{V_m\,(\text{Gas})} * V_{Headspace} \quad (2)$$

3. Results and discussion

3.1. Characterization

We synthesized g-C_3N_4 (CN) from melamine by using simple polycondensation reaction. N-doped porous carbon (NCZ) was synthesized from ZIF-8 via carbonization followed by KOH activation (Fig. 1). The reaction paths for CN formation beginning from melamine and the effect of pH on CN in zeta potential have been discussed earlier by Zhu et al. [39]. Similar to many other compounds, CN exhibits protonation and deprotonation in aqueous suspensions. This is mainly due to the interactions among hydrogen ions, hydroxyl ions, and certain functional groups present on the surface of CN. Under the prevailing pH conditions, the degree of these chemical interactions varies, thereby CN samples can possess diverse surface charges and zeta potentials.

In order to investigate the surface charges of the samples in aqueous suspensions, their zeta potentials were measured. In the original suspension without any pH adjustment (i.e., pH ~ 7), the zeta potentials of CN and NCZ were − 18.3 and − 17.9 eV, respectively. The zeta potentials of CN and NCZ as functions of the pH value of the suspensions are given in Fig. 2a. As can be seen, the zeta potential of both materials continuously increases as the pH decreases, covering the range from −20 mV to 20 mV. Here at normal preparation conditions, both precursor materials (CN and NCZ) showed negative zeta potential values, whereas at lower pH, both materials showed positive zeta potential values. In an aqueous environment, amine groups of CN could act as proton acceptors at lower pH and can provide positive charges to the surface. The negative zetapotential at neutral pH is mainly due to the presence of lone pair electrons on nitrogen in the heterocycle rings of CN. Furthermore, at higher pH, the nitrogen rich heterocycle leads to deprotonation of the primary and secondary amine groups, resulting in the negative zeta potential on the CN surface [40]. The presence of functional groups such as amine groups on the surface of the catalyst was later confirmed by IR and XPS. In the case of N-doped porous carbon (NCZ), in acidic conditions, there will be a higher concentration of H + ions, which can protonate the hydroxyl group of NCZ, resulting in a

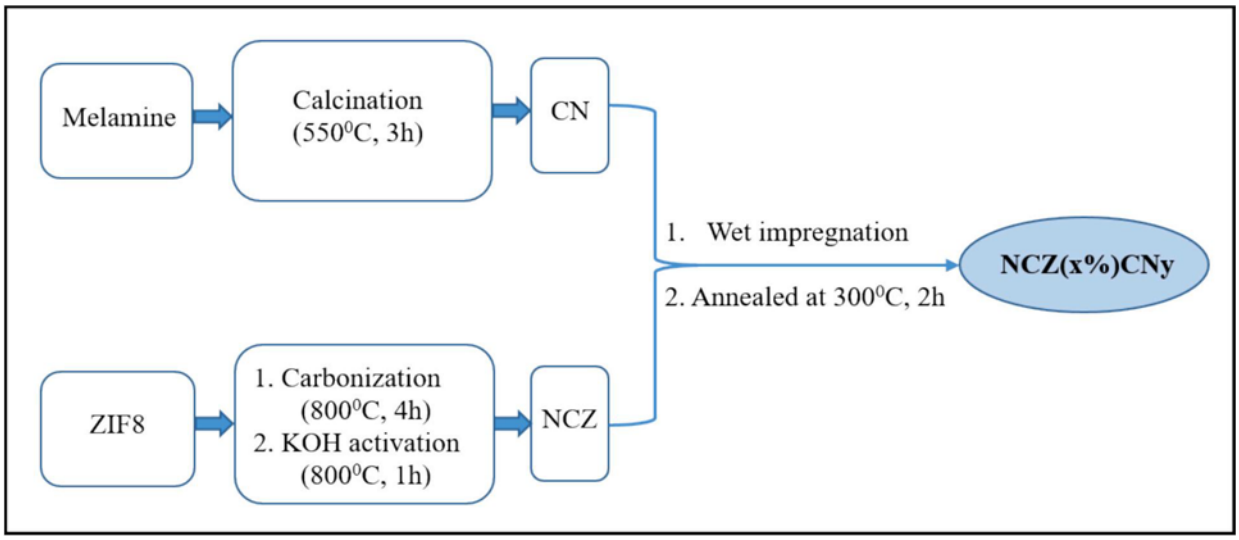

Fig. 1. Scheme: Synthesis of NCZ(x%)CNy.

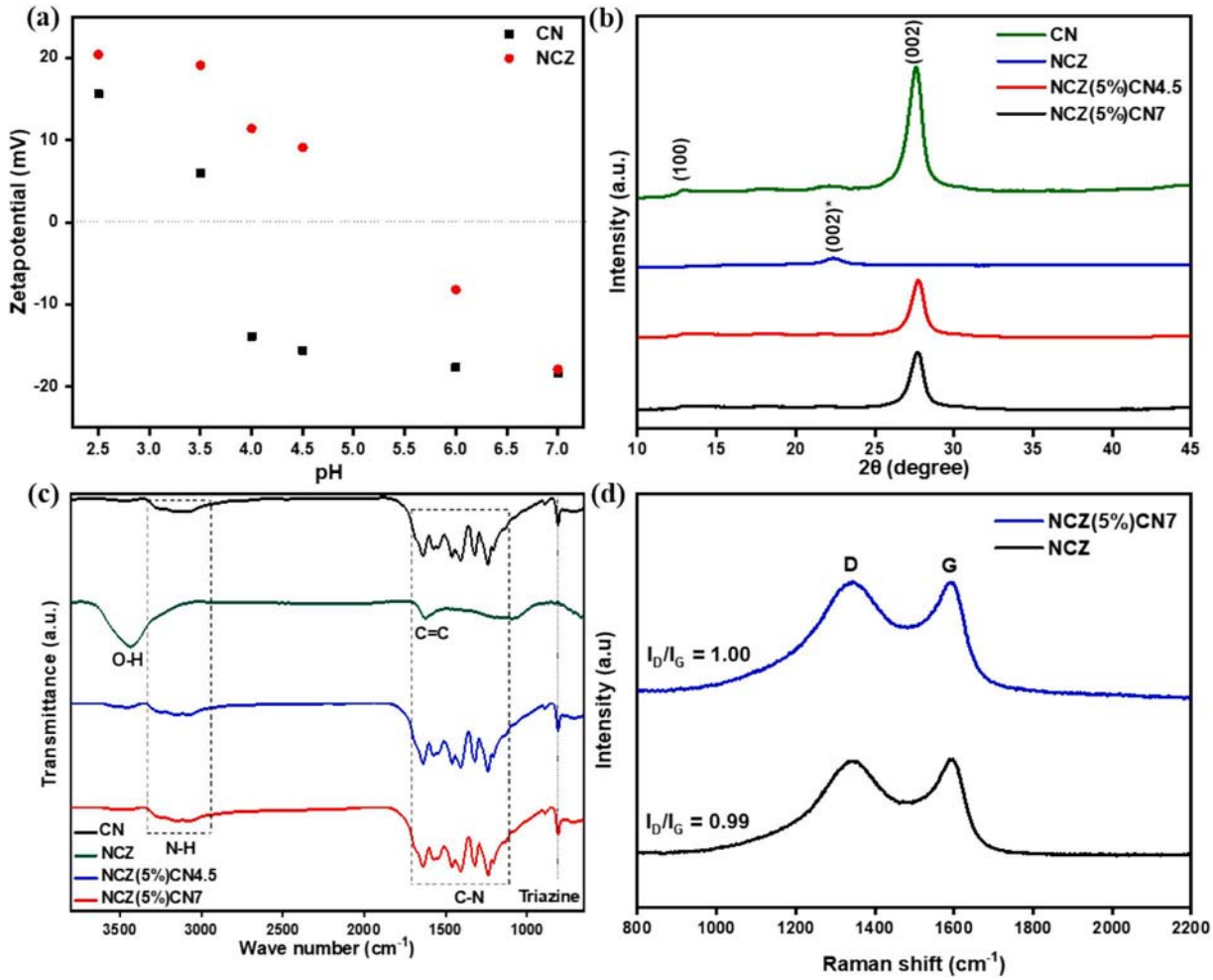

Fig. 2. (a) Zeta potential values of CN, and NCZ as a function of the pH value of the suspensions, (b) XRD pattern, (c) FTIR spectra, and (d) Raman spectra of as-synthesized materials.

positively charged surface. Whereas the negative zeta potential can be due to the presence of free lone pair electrons on nitrogen in the N-doped porous carbon. However, within a particular pH range (4 and 4.5), NCZ showed a positive value while CN had a negative value of zeta potential. We optimized and chose pH 4.5 as the synthesis condition where CN and NCZ have opposite surface charges with zeta potential values of −15.6 mV and 9.1 mV, respectively. Apart Van der Waals interaction, this surface charge difference may also help in the formation of the

composite by electrostatic interaction. As indicated in Fig. 2a, the behaviour of nanoparticles and their agglomeration is greatly influenced by the pH level of the suspension, which in turn affects the different properties such as adsorption and optical properties [41]. Due to the difference in zeta potential values at various pH conditions, we synthesized CN composites with a 5 % loading of N-doped carbon at pH 4.5 and the normal pH of 7 to study the effect of pH on composite formation and its impact on photocatalytic activity. These composites are denoted as NCZ(5 %)CN4.5 and NCZ(5 %)CN7, respectively, covering a reasonable pH range.

The crystallinity and crystal phases were analyzed by XRD (Fig. 2b). For NCZ, the characteristic diffraction peak at 2θ value of 22.4° was assigned to the (002) plane of carbon [42]. The weak diffraction peak located at about 13° corresponding to the (100) in-plane structural packing motifs of s-triazine ring units and a strong one at 27.6° can be attributed to the (002) interlayer stacking reflection of the conjugated aromatic systems in CN [43,44]. The presence of the same diffraction peaks in composites indicates the existence of CN in the composites, however this peak is broader compared to CN. The increase in the carbon content of the composites can cause a reduction in the peak intensity [35,36]. Here, the (002) peak intensity of NCZ(5 %)CN4.5 and NCZ(5 %)CN7 were less than that of CN, which confirms that the successful incorporation of carbon into CN. In addition, there are no typical diffraction peaks of carbon, which is possibly due to the formation of amorphous carbon.

The FTIR tests were performed to determine the chemical structure

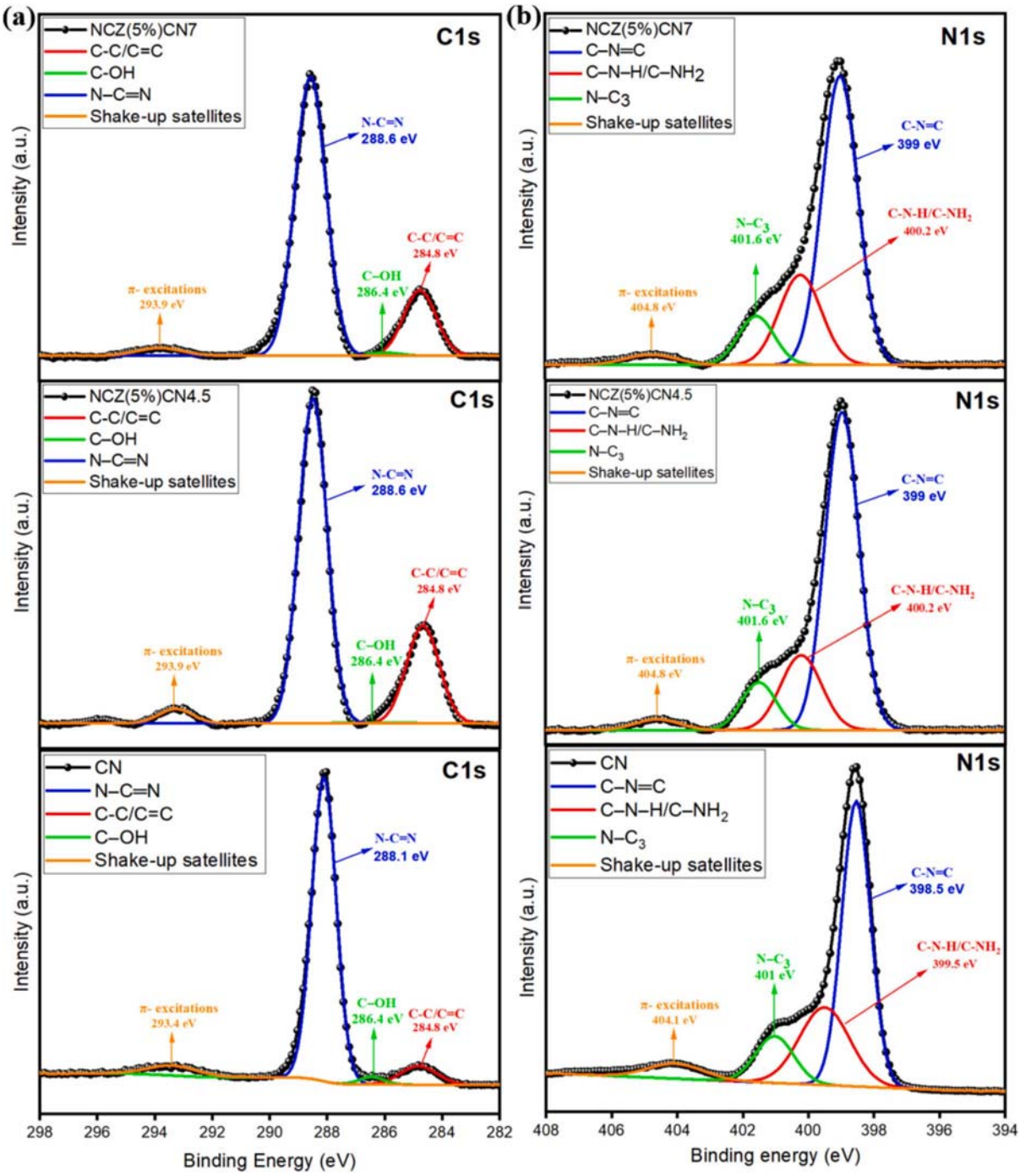

Fig. 3. XPS spectra for CN, NCZ(5 %)CN4.5 and NCZ(5 %)CN7 (a) C 1s, (b) N 1s.

and functional groups of the samples. Fig. 2c represents the spectra of CN, NCZ, NCZ(5 %)CN4.5 and NCZ(5 %)CN7. From the spectra, it is clear that there is no difference in the IR vibrational modes for all samples. The sharp peak at 811 cm^{-1} is due to the characteristic breathing mode of triazine unit of CN which can also be seen unaffected in the composites. A series of strong absorption peaks in the range of 1200—1700 cm^{-1} in CN and composites corresponds to the typical stretching modes of CN heterocycles [46]. A broad peak around 3200 cm^{-1} was observed in CN as well as in composites, which indicates the N-H stretching vibration modes. In the case of NCZ, the presence of the characteristic peaks at 3436 cm^{-1} and 1630 cm^{-1} were attributed to O-H and C=C functional groups, respectively [47,48].

Raman spectroscopy was conducted to examine the ordered structure of the carbon matrix in the catalyst. As shown in Fig. 2d, two characteristic peaks were observed at 1343 cm^{-1} and 1591 cm^{-1}, corresponding to the D-band and G-band, respectively. The extent of defects in carbon materials is typically assessed using the D/G intensity ratio (I_D/I_G). The Raman spectra revealed I_D/I_G values of 1.00 for the composite NCZ(5 %)CN7 and 0.99 for NCZ, indicating that the incorporation of N-doped carbon into g-C_3N_4 does not significantly alter the defect density or graphitic structure. This structural preservation can facilitate the synergistic contribution of N-doped carbon to the composite's photocatalytic performance without compromising its intrinsic properties.

X-ray photoelectron spectroscopy (XPS) was performed to analyze the variation in chemical compositions and chemical states of sample surfaces, and the results are shown in Fig. 3. XPS spectra of all three samples CN, NCZ(5 %)CN4.5, and NCZ(5 %)CN7 confirmed the presence of C 1 s, N 1 s and O 1 s (Fig. S2). The weak O 1 s peak (~534 eV) probably came from the adsorbed water on the surface of the samples. After the deconvolution, the C 1 s spectra show four peaks for all materials. The first one at 284.8 eV is attributed to sp^2 graphitic C=C bonds from the sample or adventitious carbon (C–C) from the instrument [45]. The second one at 286.4 eV is assigned to hydroxyl groups (C–OH). In the case of CN, the third and fourth peaks situated at 288.1 eV and 293.4 eV are attributed to sp^2 carbons (π- excitations) of heptazine rings and shake-up satellite, respectively [36]. Contrary to the CN peaks, the composites (NCZ(5 %)CN4.5, and NCZ(5 %)CN7) showed a very small shift of ~0.5 eV for the same peaks (288.6 eV and 293.9 eV), which can be due to the carbon incorporation. For CN, the N 1 s spectra show overall four peaks. The main peak deconvoluted at 398.5, 399.5, and 401 eV are assigned to sp^2 nitrogen on the heptazine ring (C=N–C), amino groups (C–NH_2 or C–NH–), and a central nitrogen singly bonded to three carbons N–$(C)_3$, respectively. There is another final peak at 404.1 eV, which originated from the shake-up satellite and is attributed to charging effects [36,49]. It was observed that a small peak shift happened for composites with peaks at 399, 400.2, 401.6, and 404.8 eV corresponding to the same groups as above.

In order to investigate the vacancies and active species involved in the photocatalytic CO_2 reduction mechanism, EPR spectroscopy was employed. EPR spectra of CN, and NCZ(5 %)CN7 were studied at room temperature, and the absorption lines revealed a narrow, symmetrical signal of Lorentzian shape at g = 2.0037 and g = 2.0029, respectively (Fig. 4a and 4b). Upon illumination with LED lamp (a high-power white flashlight), a slight change in the intensity and line width of the signal is

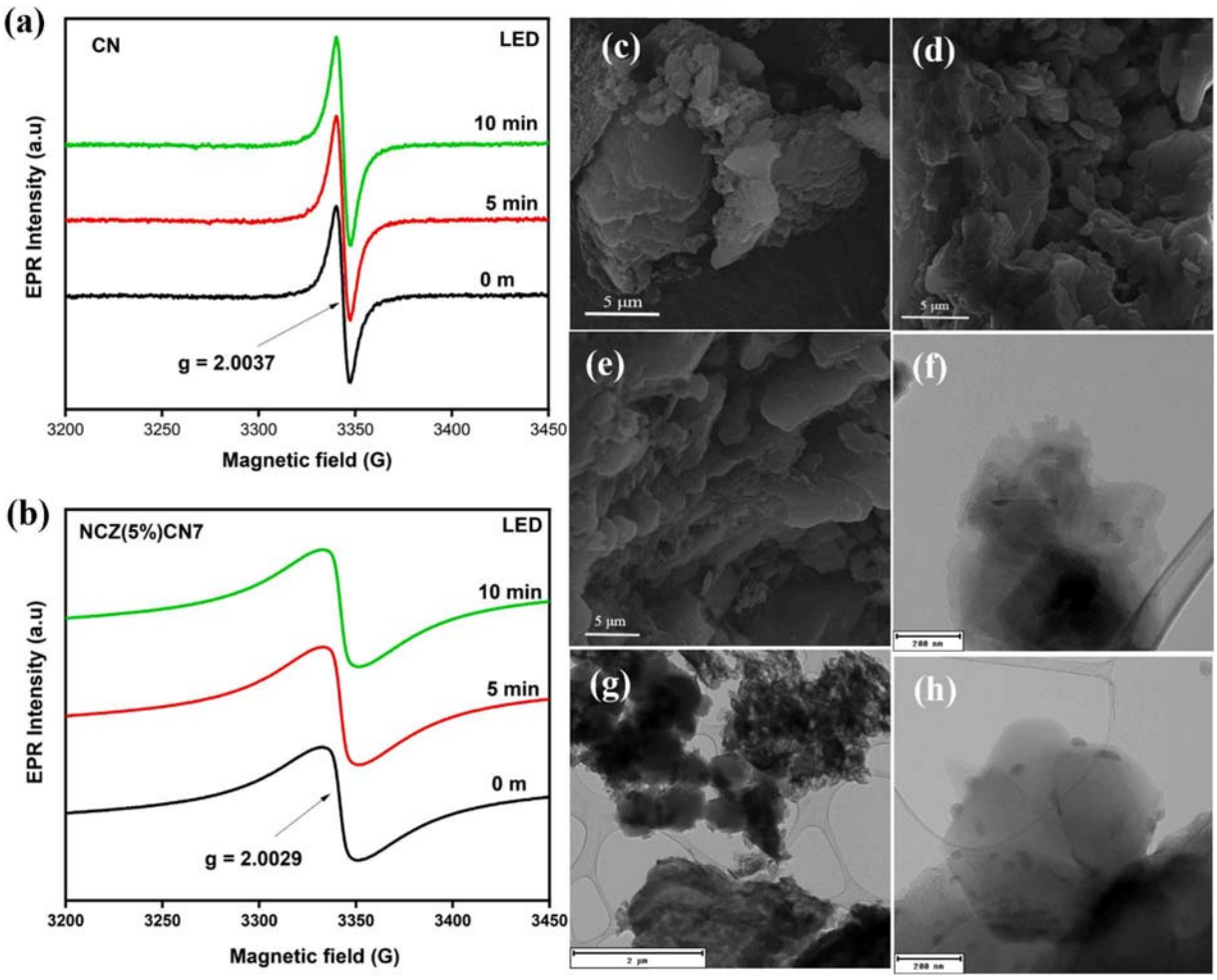

Fig. 4. EPR spectra for (a) CN and (b) NCZ(5%)CN7, SEM images of (c) CN, (d) NCZ(5%)CN4.5, and (e) NCZ(5%)CN7, and TEM images of (f) CN, (g) NCZ(5%)CN4.5, and (h) NCZ(5%)CN7.

observed. Simulations in EasySpin confirm these changes (Fig. S3), indicating the photoinduced generation of charge carriers and consequently the formation of reactive oxygen species. The study by Gong et al. [50] confirmed that carbon vacancies in g-C_3N_4 help separate photoinduced charges and can be detected by the EPR method. The detected g-values of our materials correspond to characteristic parameters of carbon/nitrogen vacancies and unpaired electrons, commonly associated with the formation of superoxide radicals ($O_2\bullet^-$) [51–53]. The slight shift in g-value for the NCZ(5 %)CN7 composite further suggests a modified electronic environment due to N-doped carbon incorporation, enhancing charge separation and facilitating radical formation. These results align well with prior findings on g-C_3N_4-based materials, where carbon/nitrogen vacancies serve as electron traps aiding in superoxide generation [54,55]. While •OH and h^+ radicals may still be present, the dominance of $O_2\bullet^-$ as the main reactive species is supported by both the EPR data and thermodynamic favorability [56–58].

In order to study the thermal stability of the materials, we carried out thermogravimetric (TG) analysis in the air. The TGA results (Fig. S4) confirmed that the precursors as well as the composites exhibited good thermal stability up to about 550 – 600 °C. Therefore, the annealing temperature of 300 °C applied during the synthesis did not negatively affect the composite formation, as evidenced by the composite yield.

The morphology of CN and composites were investigated by SEM and TEM. SEM images (Fig. 4c-e) revealed that CN exhibits a sheet-like layered structure, while NCZ (Fig. S5) displayed well-defined polyhedral structures. In order to confirm the morphology and structure, TEM analysis (Fig. 4f-h) was also performed. The black dots in the composite (Fig. 4 h) indicate the presence of NCZ on CN, which further confirmed the successful incorporation of NCZ and CN. The presence of carbon and nitrogen in the composite was confirmed by EDS elemental mapping (Fig. S6).

N_2 adsorption–desorption measurements were used to investigate the pore structure and specific surface area of the as-synthesized materials. The BET specific surface area of materials was measured, and the observed isotherms exhibited a type IV curve (Fig. 5a), which is indicative of the catalysts' mesoporous nature. Both composite materials NCZ (5 %)CN4.5 and NCZ(5 %)CN7 showed almost same surface area of 151.4 m^2/g and 155.2 m^2/g, respectively, which is obvious because of the same amount of NCZ loading. Interestingly, these values of surface areas of the composites are around 54 times higher than that of the base material, CN (2.85 m^2/g). This immense enhancement in the surface area of composites is mainly due to the incorporation of high surface area material NCZ (2729.7 m^2/g), which also indicates that it is favorable to generate more active sites on the surface. In order to study the CO_2 capturing capacity of the materials, we also carried out CO_2 adsorption measurements at 0 °C. For the photocatalytic reduction of CO_2, materials having higher CO_2 capturing capacity are vital. It is already reported that nitrogen doping can enhance the CO_2 adsorption capacity of a material [59]. From Fig. 5b, it is clear that the composites showed higher CO_2 capturing capacity than CN (0.08 mmol/g). CO_2 capacity of NCZ(5 %)CN4.5 is 4 times higher than that of CN whereas NCZ(5 %)CN7 shows 3.5 times higher value. Overall, the adsorption studies confirm that compared to the base material CN, the composites exhibited higher surface area along with good CO_2 adsorption capacity, which is crucial for the photocatalytic reduction of CO_2.

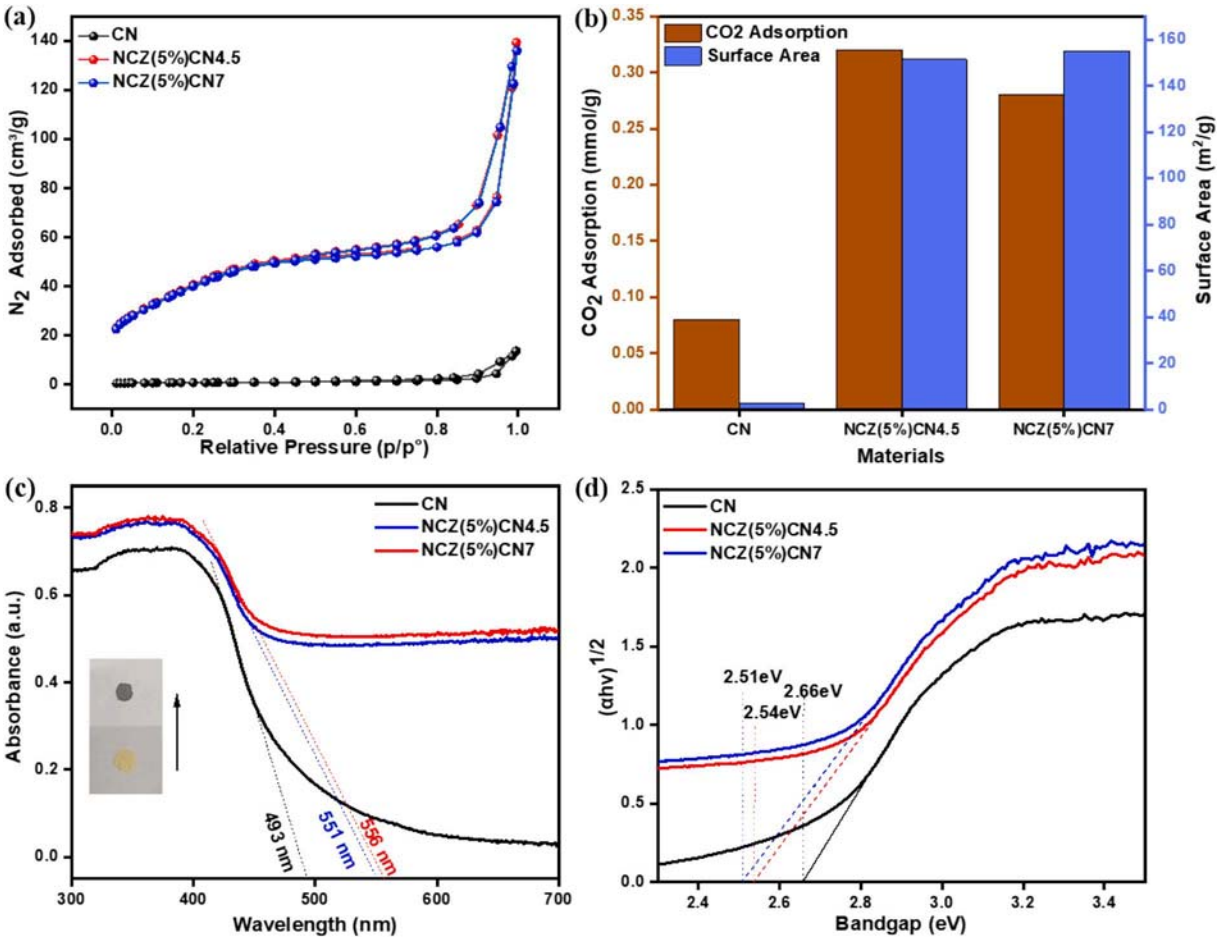

Fig. 5. (a) N_2 adsorption–desorption isotherm, (b) CO_2 adsorption and surface area comparison (c) DRS UV–Vis spectra, and (d) Optical band gap energy evaluation of as synthesized materials.

The optical absorption properties of as-prepared samples were analyzed by UV–Vis diffuse reflectance spectroscopy. Fig. 5c shows the DRS UV–Vis absorption curves of CN, NCZ(5 %)CN4.5 and NCZ(5 %) CN7. The spectrum shows that the light absorption wavelength of CN, NCZ(5 %)CN4.5 and NCZ(5 %)CN7 are 518 nm, 551 nm and 556 nm, respectively, which are within the visible light range. The absorption spectra of the composites exhibited a redshift and a slight increase in intensity compared to CN. This shift and increase of the peak intensity were ascribed to the presence of doped carbon, which aligns with the observed change in sample color from yellow (for CN) to grey (for composites). The large-scale practical use of CO_2 photoreduction is limited due to the poor conversion efficiency of many photocatalysts. One of the major reasons for this obstacle is the inefficient utilization of solar energy. The optical bandgap of a material affects its ability to absorb light and generate electron hole pairs, which are essential for photocatalytic activity. Generally, narrow band gap materials allow the absorption of light in the visible region, which constitutes a higher percentage of solar light. Also, introduction of carbon elements into CN can accelerate the interfacial charge-carrier separation as well as reduction in the bandgap as evidenced from previous studies [26,34,35,60]. Our materials showed an indirect band gap, which was obtained using the Kubelka-Munk theory. From tauc plot, the corresponding bandgaps were determined to be 2.66 eV for CN, 2.54 eV for NCZ(5 %)CN4.5, and 2.51 eV for NCZ(5 %)CN7 (Fig. 5d). The reduction in bandgap can be due to the porous carbon incorporation with CN as mentioned earlier and this narrow band gap allows the material to absorb large portion of solar spectrum including visible light, which is also useful for direct sunlight utilization [61].

Photoluminescence (PL) spectra are widely used to study the effective generation, separation, and migration of the photo-generated electron–hole pairs in a semiconductor. This is because photo luminescent emissions result from the recombination of these free carriers [62]. The PL spectra of as-prepared samples at room temperature with an excitation wavelength of 410 nm are shown in Fig. 6a. All samples exhibited similar emission trends with a strong emission peak at 483 nm, which can be attributed to recombination of electron–hole pairs in the CN. The graph shows that there is a significant reduction in the PL intensity of composites compared to that of CN. The lower intensity of peak represents higher efficiency of photoinductive charge transfer and a better separation of photogenerated charge carriers, hence a lower recombination probability [63]. It can be inferred that the carbon doped composite can well block the recombination of photogenerated electron hole pairs, indicating a special path for carrier transport between C_3N_4 and NCZ [64]. Also, NCZ acts as a good electron-acceptor material to effectively promote the electron-hole pairs separation [45,65]. Therefore, composites enable their use as highly promising catalysts for sunlight-driven photocatalytic applications.

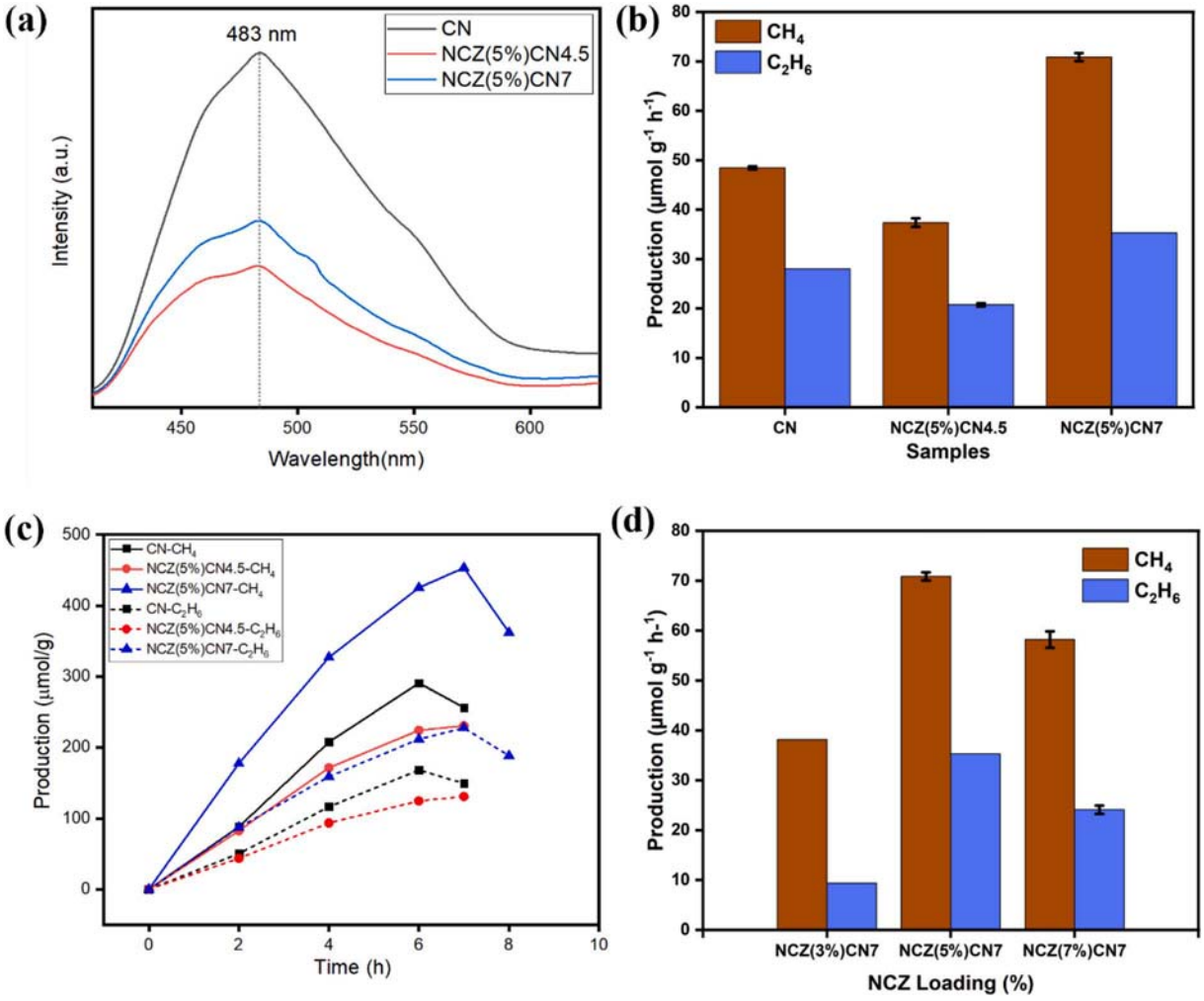

Fig. 6. (a) PL spectra for CN, NCZ(5%)CN4.5, and NCZ(5%)CN7, (b)&(d) Production yield comparison of the photocatalytic CO_2 reduction of as-prepared samples, and (c) Production rate of CO_2 reduction.

3.2. Photocatalytic performance

3.2.1. Enhanced photocatalytic activity of NCZ(5 %)CN7 under visible light irradiation

The photocatalytic CO_2 reduction performance of the samples in the liquid phase was evaluated under simulated solar light irradiation. Control experiments confirmed that no hydrocarbons were produced in the absence of either the photocatalyst or light, which demonstrates that CO_2 reduction can only occur when both the catalyst and light are present simultaneously. In experiments, photocatalysts were used under identical conditions, no carbon-based products were detected unless CO_2 was supplied. This indicates that CO_2 is the exclusive carbon source for the reaction. The reduction products were identified as methane and ethane (Table S1). As a clean-burning fuel and drop-in replacement for natural gas, CH_4 is an ideal product of CO_2 photoreduction. Similarly, ethane is a crucial feedstock for the petrochemical industry and can be used as a fuel [66,67]. The development of highly active and stable metal-free semiconductor-based photocatalysts for this important transformation has been really challenging. Fascinatingly, the prepared composite (NCZ(5 %)CN7) showed better conversion efficiency compared to previous reports (Table S2). Also, comparative studies indicate that CO_2 reduction is predominantly investigated under UV light. However, in this work, a solar simulator was utilized to replicate the broader spectrum of sunlight, offering a more realistic evaluation of photocatalytic performance.

Fig. 6b displays a production yield comparison of the photocatalytic CO_2 reduction of as-prepared samples, while Fig. 6c depicts the production rate of CO_2 reduction products (CH_4 and C_2H_6) for each composite along with CN. Interestingly, it was observed that the composite at neutral pH (NCZ(5 %)CN7) showed higher activity (CH_4 – 70.87 μmol $g^{-1}h^{-1}$, C_2H_6 – 35.31 μmol $g^{-1}h^{-1}$) compared to the other materials, whereas the composite at pH 4.5 (NCZ(5 %)CN4.5) showed the lowest, even lower than CN (CH_4 – 48.48 μmol $g^{-1}h^{-1}$, C_2H_6 – 28.04 μmol $g^{-1}h^{-1}$). The photocatalytic CO_2 reduction activity follows the order NCZ (5 %)CN4.5 < CN < NCZ(5 %)CN7. As mentioned earlier in the adsorption studies, the composites showed higher surface area as well as CO_2 capturing capacity than that of CN, which can be the reason for the higher activity of NCZ(5 %)CN7 than CN. However, the lower catalytic activity of NCZ(5 %)CN4.5 implies that factors other than surface area and adsorption are limiting the photocatalytic reduction reaction. It is already reported that the photocatalytic activity of the photo catalyst can be notably affected by the pH conditions employed during the synthesis process [68]. The pH during synthesis plays a crucial role in shaping the morphology of the photo catalyst, influencing the surface of the catalyst, and thereby impacting photocatalytic performance [69–71]. The effect of pH on surface charge was studied and explained earlier in the zeta potential section. In our case, during synthesis, at lower pH 4.5, N-containing functional groups such as amine and hydroxyl groups on the surface of the catalyst can get protonated, which affects the orientation of active sites. This can reduce their effectiveness in interacting with CO_2. This may affect the availability of CO_2 for the reduction process, thus lesser CO_2 reduction product yield. In the case of NCZ(5 %)CN7, the surface of the catalyst was not affected by H^+ during synthesis. Thus, all the active sites were unaffected by H^+ and available for the CO_2 adsorption and photocatalytic conversion of CO_2. As mentioned earlier, the optical band gap of NCZ(5 %)CN7 is slightly lower than NCZ(5 %)CN4.5 also supports the photocatalytic activity results.

Based on characterization results, we propose a possible charge carrier migration pathway at the heterojunction interface between CN and NCZ during photocatalytic CO_2 reduction. When exposed to sunlight, electrons in CN are excited from the valence band (VB) to the conduction band (CB), leaving behind photogenerated holes (h^+) in the VB. The excited electrons (e^-) then migrate through the conduction band. N-doped porous carbon (NCZ) plays a crucial role by enhancing CO_2 adsorption, bringing the molecules closer to the catalyst surface for efficient reduction. Additionally, it improves charge separation, preventing electron-hole recombination. The photogenerated electrons react with molecular oxygen (O_2) adsorbed on the catalyst surface, generating superoxide radicals ($O_2\bullet^-$). These radicals drive a series of reduction reactions that convert CO_2 into CH_4 and C_2H_6. The EPR analysis confirms that $O_2\bullet^-$ radicals are the primary active species responsible for CO_2 reduction, further validating this reaction mechanism.

3.2.2. Impact of carbon loading on composite performance

From the above results, we conclude that the composite synthesized at neutral pH (NCZ(5 %)CN7) had the highest activity. In order to study the effect of carbon incorporation on conversion efficiency, we carried out experiments with 3 % and 7 % loading of N-doped carbon for comparison with 5 % loading (Fig. 6d). The results confirmed that NCZ (5 %)CN7 showed higher activity than 3 % and 7 % loading, which means that there is an optimum carbon loading, which is needed for a composite to show good activity. When the amount of carbon increases past a certain amount, the active sites of CN can be masked by carbon, reducing the overall efficiency. Similarly, lower amounts of carbon loading will not be sufficient to enhance the surface area of the material, which can ultimately affect the CO_2 adsorption capacity. This is why an optimum amount of carbon loading is needed. In this study, we found that a loading of 5 % NCZ into CN is the optimum, which we further confirmed by photoluminescence studies (Fig. S7), and the results match with the photocatalytic activity results. Newly synthesized composites showing the same chemical composition and crystallinity of NCZ(5 %) CN7, which we confirmed by IR and XRD are shown in the supporting information (Fig. S8 and S9).

We also carried out optical band gap studies for newly synthesized composites. The optical band gap results (Fig. S10) are consistent with the CO_2 reduction performance results. NCZ(3 %)CN showed a higher band gap of 2.58 eV and NCZ(7 %)CN with 2.54 eV, whereas NCZ(5 %) CN has the lowest band gap energy of 2.51 eV, which allows the absorption of a wide range of light, hence the higher photocatalytic activity.

3.2.3. Electrochemical insights into photocatalytic performance

To further investigate the cause of the enhanced photocatalytic performance, photocurrent measurements and electrochemical impedance spectroscopy (EIS) were conducted. These analyses are crucial for revealing the separation efficiency of photo-generated electron-hole pairs. The linear sweep voltammogram (LSV) polarization curves (Fig. 7a) showed that the composite NCZ(5 %)CN7 has a current density of −0.73 mA.cm^{-2}, which is higher than that of CN (−0.46 mA.cm^{-2}). This promoted photocurrent density results illustrate that in the case of NCZ(5 %)CN7 more electrons are being created and transferred. In the EIS Nyquist plot (Fig. 7b), the semicircle in the high-frequency region is typically attributed to charge transfer resistance. A smaller semicircle diameter indicates more effective charge carrier migration, reduced resistance, and a lower recombination rate of electron-hole pairs, thereby enhancing conductivity [72,73]. Here, CN exhibited an enlarged semicircle, whereas the radius of NCZ(5 %)CN7 was much smaller, suggesting that NCZ(5 %)CN7 has lower charge transfer resistance, indicative of better charge separation and transfer. The results were in accordance with the observed PL spectra, optical bandgaps, photocurrent responses, and enhanced photocatalytic CO_2 reduction performance. These electrochemical measures also confirm that the introduction of N-doped porous carbon in CN is an effective strategy to accelerate the interfacial charge-carrier separation.

3.2.4. Structural influence on photocatalytic performance

Overall, the photocatalyst NCZ(5 %)CN7 composite not only has the advantages of individual components but also has stronger catalytic ability than the two monomers due to the synergistic effect of NCZ and CN. In the composite, the main photocatalytic component is CN. Then

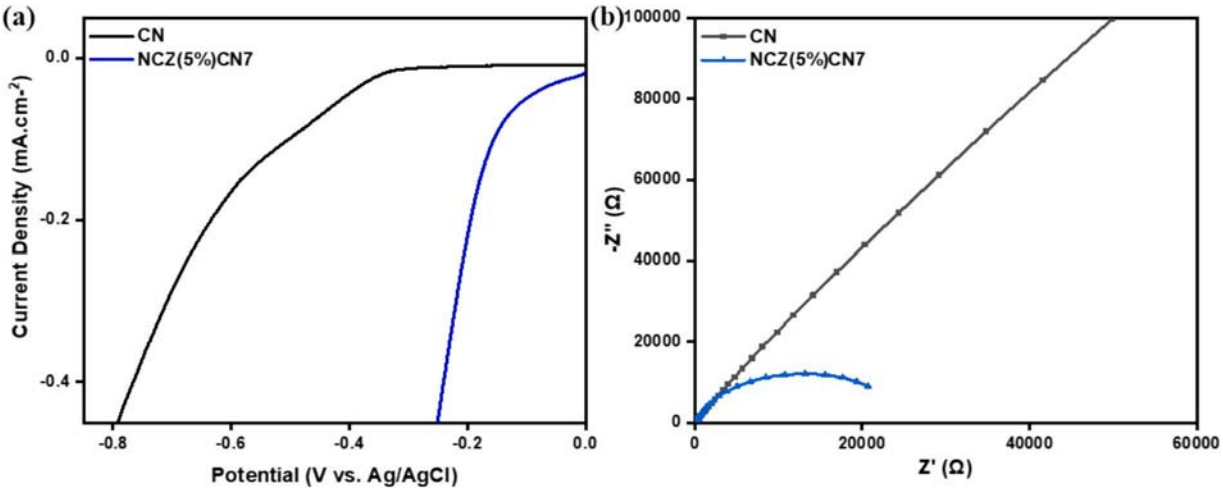

Fig. 7. (a) Linear Sweep voltammogram (LSV) polarization curves, and (b) Nyquist plot.

the incorporation of NCZ provides a higher surface area, creating more active sites in the catalyst, and a lower optical bandgap helps to absorb a large portion of sunlight. Additionally, the presence of N-doped porous carbon also helps in the enhancement of CO_2 adsorption characteristics. From the electrochemical experimental results, the improvement of the photocatalytic performance also influenced by the fast separation and transfer of photo-generated electron-hole pairs, is mainly caused by the existence of the hierarchical porous carbon [74]. This structural synergy leads to a remarkable improvement in photocatalytic activity, facilitating the efficient reduction of CO_2 into valuable products like CH_4 and C_2H_6.

A previous study from our group [36] investigated a g-C_3N_4-based photocatalyst with N-doped carbon under similar reaction conditions for the photocatalytic degradation of methylene blue. The study demonstrated good stability over multiple cycles, highlighting the robustness of N-doped carbon-supported g-C_3N_4 photocatalysts. Additionally, SEM and XRD analyses of the optimized photocatalyst (NCZ(5 %)CN7) after the photocatalytic reaction were obtained to confirm the stability of the material. Post-reaction SEM images (Fig. S11) confirm that the photocatalyst maintains its morphology without significant structural collapse or agglomeration. The comparison of XRD patterns (Fig. S12) before and after the reaction shows that the catalyst retains its crystalline structure, indicating phase and structure stability.

4. Conclusions

In summary, a novel metal-free photocatalyst NCZ(5 %)CN7 was successfully synthesized through the integration of N-doped hierarchically porous carbon into melamine-derived g-C_3N_4 by a simple wet synthesis method. The synergistic interaction between NCZ and CN in the composite results in a narrowed bandgap, an extended light response range, enhanced charge carrier migration due to the reduced electron-hole recombination rate, increased surface area, and improved CO_2 adsorption capacity, collectively leading to enhanced photocatalytic activity. Compared to g-C_3N_4, the optimized photocatalyst NCZ(5 %)CN7 exhibited a 54-fold increase in surface area, a 3.5-fold enhancement in CO_2 adsorption, and significantly improved photocatalytic activity for CO_2 reduction, achieving a maximum CH_4 production rate of 70.87 μmol h^{-1} g^{-1} and a C_2H_6 production rate of 35.31 μmol h^{-1} g^{-1}. The results confirm that our developed material has the potential to keep the global carbon balance and meet the energy demand for industrial applications with a single novel catalyst. This can also be a great initiation and provide insights into the cost-effective CO_2 utilization in the modern era of industrial applications.

CRediT authorship contribution statement

Roopesh Mekkat: Writing – original draft, Visualization, Validation, Methodology, Investigation, Conceptualization. **Edith Mawunya Kutorglo:** Methodology, Conceptualization. **Milena Setka:** Methodology, Conceptualization. **Andrey. Prokhorov:** Data curation, Writing – review & editing. **Miroslav Šoóš:** Writing – original draft, Visualization, Validation, Methodology, Investigation, Conceptualization.

Declaration of competing interest

The authors declare that they have no known competing financial interests or personal relationships that could have appeared to influence the work reported in this paper.

Acknowledgements

The authors gratefully acknowledge the support from the Technology Agency of the Czech Republic and the research council of Norway through the project METAMORPH (EEA & Norway Grant project TO01000329), Grant agency of Czech Republic GAČR 24-12812S, the specific university grant (A2_FCHI_2023_030) & (A2_FCHI_2024_040) and Dr. Balamurugan Devadas for his support in electrochemical analysis. E. M. K. is grateful to the European Structural and Investment Funds OP RDE-funded project 'CHEMFELLS IV' (Project No. CZ.02.2.69/0.0/0.0/20_079/0017899) for funding.

Appendix A. Supplementary data

Supplementary data to this article can be found online at https://doi.org/10.1016/j.jphotochem.2025.116454.

Data availability

Data will be made available on request.

References

[1] IEA (2022), World Energy Outlook 2022, IEA, Paris https://www.iea.org/reports/world-energy-outlook-2022, License: CC BY 4.0 (report); CC BY NC SA 4.0 (Annex A), n.d.
[2] V. Kumaravel, J. Bartlett, S.C. Pillai, Photoelectrochemical Conversion of Carbon Dioxide (CO 2) into Fuels and Value-Added Products, ACS Energy Lett. 5 (2020) 486–519, https://doi.org/10.1021/acsenergylett.9b02585.
[3] F. Nocito, A. Dibenedetto, Atmospheric CO2 mitigation technologies: carbon capture utilization and storage, Curr. Opin. Green Sustain. Chem. 21 (2020) 34–43, https://doi.org/10.1016/j.cogsc.2019.10.002.

[4] E. Martin-Roberts, V. Scott, S. Flude, G. Johnson, R.S. Haszeldine, S. Gilfillan, Carbon capture and storage at the end of a lost decade, One Earth 4 (2021) 1569–1584, https://doi.org/10.1016/j.oneear.2021.10.002.

[5] T. Singh, A. Arpanaei, D. Elustondo, Y. Wang, A. Stocchero, T.A.P. West, Q. Fu, Emerging technologies for the development of wood products towards extended carbon storage and CO2 capture, Carbon Capture Sci. Technol. 4 (2022) 100057, https://doi.org/10.1016/j.ccst.2022.100057.

[6] H. Yamada, Amine-based capture of CO2 for utilization and storage, Polym. J. 53 (2021) 93–102, https://doi.org/10.1038/s41428-020-00400-y.

[7] E. Gong, S. Ali, C.B. Hiragond, H.S. Kim, N.S. Powar, D. Kim, H. Kim, S.-I. In, Solar fuels: research and development strategies to accelerate photocatalytic CO $_2$ conversion into hydrocarbon fuels, Energy Environ. Sci. 15 (2022) 880–937, https://doi.org/10.1039/D1EE02714J.

[8] Y.-Y. Lin, F.-Y. Liu, I.-C. Chen, H.-Y. Tsai, J.-W. Huang, J.-H. Lin, C.-C. Chen, Photocatalytic reduction of carbon dioxide by BiTeX (X = Cl, Br, I) under visible-light irradiation, J. Environ. Manage. 365 (2024) 121536, https://doi.org/10.1016/j.jenvman.2024.121536.

[9] U. Ghosh, A. Majumdar, A. Pal, Photocatalytic CO2 reduction over g-C3N4 based heterostructures: Recent progress and prospects, J. Environ. Chem. Eng. 9 (2021) 104631, https://doi.org/10.1016/j.jece.2020.104631.

[10] X. Li, J. Xiong, X. Gao, J. Huang, Z. Feng, Z. Chen, Y. Zhu, Recent advances in 3D g-C3N4 composite photocatalysts for photocatalytic water splitting, degradation of pollutants and CO2 reduction, J. Alloys Compd. 802 (2019) 196–209, https://doi.org/10.1016/j.jallcom.2019.06.185.

[11] Q. Zhu, Z. Li, T. Zheng, X. Zheng, S. Liu, S. Gao, X. Fu, X. Su, Y. Zhu, Y. Zhang, Y. Wei, High-Selectivity Tandem Photocatalytic Methanation of CO_2 by Lacunary Polyoxometalates-Stabilized *CO Intermediate, Angew. Chem. Int. Ed. 64 (2025) e202413594, https://doi.org/10.1002/anie.202413594.

[12] H.-L. Chen, C.-S. Lu, F.-Y. Liu, Y.-Y. Lin, C.-C. Chen, D. Zou, Efficiency of CO2 photoreduction to hydrocarbons with K2Fe2O4/rGO heterojunction as a photocatalyst, J. CO2 Util. 85 (2024) 102858, https://doi.org/10.1016/j.jcou.2024.102858.

[13] Z. Ren, F. Chen, K. Wen, J. Lu, Enhanced photocatalytic activity for tetracyclines degradation with Ag modified g-C3N4 composite under visible light, J. Photochem. Photobiol. Chem. 389 (2020) 112217, https://doi.org/10.1016/j.jphotochem.2019.112217.

[14] J. Wen, J. Xie, X. Chen, X. Li, A review on g-C 3 N 4 -based photocatalysts, Appl. Surf. Sci. 391 (2017) 72–123, https://doi.org/10.1016/j.apsusc.2016.07.030.

[15] S. Ye, R. Wang, M.-Z. Wu, Y.-P. Yuan, A review on g-C3N4 for photocatalytic water splitting and CO2 reduction, Appl. Surf. Sci. 358 (2015) 15–27, https://doi.org/10.1016/j.apsusc.2015.08.173.

[16] Z. Sun, H. Wang, Z. Wu, L. Wang, g-C3N4 based composite photocatalysts for photocatalytic CO2 reduction, Catal. Today 300 (2018) 160–172, https://doi.org/10.1016/j.cattod.2017.05.033.

[17] A. Alaghmandfard, K. Ghandi, A Comprehensive Review of Graphitic Carbon Nitride (g-C3N4)–Metal Oxide-Based Nanocomposites: Potential for Photocatalysis and Sensing, Nanomaterials 12 (2022) 294, https://doi.org/10.3390/nano12020294.

[18] Q. Ma, B. Kutilike, N. Kari, S. Abliz, A. Yimit, Study on surface sensitization of g-C3N4 by functioned different aggregation behavior porphyrin and its optical properties, Mater. Sci. Semicond. Process. 121 (2021) 105316, https://doi.org/10.1016/j.mssp.2020.105316.

[19] D. Huang, X. Sun, Y. Liu, H. Ji, W. Liu, C.-C. Wang, W. Ma, Z. Cai, A carbon-rich g-C3N4 with promoted charge separation for highly efficient photocatalytic degradation of amoxicillin, Chin. Chem. Lett. 32 (2021) 2787–2791, https://doi.org/10.1016/j.cclet.2021.01.012.

[20] Q. Wang, Z. Fang, W. Zhang, D. Zhang, High-Efficiency g-C3N4 Based Photocatalysts for CO2 Reduction: Modification Methods, Adv. Fiber Mater. 4 (2022) 342–360, https://doi.org/10.1007/s42765-021-00122-7.

[21] S. Liu, F. Chen, S. Li, X. Peng, Y. Xiong, Enhanced photocatalytic conversion of greenhouse gas CO2 into solar fuels over g-C3N4 nanotubes with decorated transparent ZIF-8 nanoclusters, Appl. Catal. B Environ. 211 (2017) 1–10, https://doi.org/10.1016/j.apcatb.2017.04.009.

[22] Y. Xu, W. Hou, K. Huang, H. Guo, Z. Wang, C. Lian, J. Zhang, D. Wu, Z. Lei, Z. Liu, L. Wang, Engineering Built-In Electric Field Microenvironment of CQDs/g-C_3 N_4 Heterojunction for Efficient Photocatalytic CO_2 Reduction, Adv. Sci. 11 (2024) 2403607, https://doi.org/10.1002/advs.202403607.

[23] M. Que, W. Cai, J. Chen, L. Zhu, Y. Yang, Recent advances in g-C $_3$ N $_4$ composites within four types of heterojunctions for photocatalytic CO $_2$ reduction, Nanoscale 13 (2021) 6692–6712, https://doi.org/10.1039/D0NR09177D.

[24] Q. Lu, K. Eid, W. Li, A.M. Abdullah, G. Xu, R.S. Varma, Engineering graphitic carbon nitride (g-C 3 N 4) for catalytic reduction of CO 2 to fuels and chemicals: strategy and mechanism, Green Chem. 23 (2021) 5394–5428, https://doi.org/10.1039/D1GC01303C.

[25] Q. Xu, Z. Xia, J. Zhang, Z. Wei, Q. Guo, H. Jin, H. Tang, S. Li, X. Pan, Z. Su, S. Wang, Recent advances in solar-driven CO $_2$ reduction over g-C $_3$ N $_4$ -based photocatalysts, Carbon Energy 5 (2023) e205.

[26] J. Dong, J. Zhao, X. Yan, L. Li, G. Liu, M. Ji, B. Wang, Y. She, H. Li, J. Xia, Construction of carbonized polymer dots/potassium doped carbon nitride nanosheets Van der Waals heterojunction by ball milling method for facilitating photocatalytic CO2 reduction performance in pure water, Appl. Catal. B Environ. Energy 351 (2024) 123993, https://doi.org/10.1016/j.apcatb.2024.123993.

[27] Y.-Y. Lin, C.-S. Lu, F.-Y. Liu, H.-H. Huang, J.-H. Lin, C.-C. Chen, Visible-light-driven photocatalysis of carbon dioxide by BiSeX and BiSeX/g-C3N4 (X = Cl, Br, I), Mater. Today Sustain. 23 (2023) 100473, https://doi.org/10.1016/j.mtsust.2023.100473.

[28] G. Singh, J. Lee, A. Karakoti, R. Bahadur, J. Yi, D. Zhao, K. AlBahily, A. Vinu, Emerging trends in porous materials for CO $_2$ capture and conversion, Chem. Soc. Rev. 49 (2020) 4360–4404, https://doi.org/10.1039/D0CS00075B.

[29] M. Sai Bhargava Reddy, D. Ponnamma, K.K. Sadasivuni, B. Kumar, A.M. Abdullah, Carbon dioxide adsorption based on porous materials, RSC Adv. 11 (2021) 12658–12681. https://doi.org/10.1039/D0RA10902A.

[30] Y. Ma, Z. Wang, X. Xu, J. Wang, Review on porous nanomaterials for adsorption and photocatalytic conversion of CO2, Chin. J. Catal. 38 (2017) 1956–1969, https://doi.org/10.1016/S1872-2067(17)62955-3.

[31] B.C.M. Martindale, G.A.M. Hutton, C.A. Caputo, S. Prantl, R. Godin, J.R. Durrant, E. Reisner, Enhancing Light Absorption and Charge Transfer Efficiency in Carbon Dots through Graphitization and Core Nitrogen Doping, Angew. Chem. 129 (2017) 6559–6563, https://doi.org/10.1002/ange.201700949.

[32] E.M. Kutorglo, F. Hassouna, A. Beltzung, D. Kopecký, I. Sedlářová, M. Šoóš, Nitrogen-rich hierarchically porous polyaniline-based adsorbents for carbon dioxide (CO2) capture, Chem. Eng. J. 360 (2019) 1199–1212, https://doi.org/10.1016/j.cej.2018.10.133.

[33] S. Wang, J. Qin, Y. Zhao, L. Duan, J. Wang, W. Gao, R. Wang, C. Wang, M. Pal, Z. Wu, W. Li, D. Zhao, Ultrahigh Surface Area N-Doped Hierarchically Porous Carbon for Enhanced CO $_2$ Capture and Electrochemical Energy Storage, ChemSusChem 12 (2019) 3541–3549, https://doi.org/10.1002/cssc.201901137.

[34] Z. Wang, N. Goyal, L. Liu, D.C.W. Tsang, J. Shang, W. Liu, G. Li, N-doped porous carbon derived from polypyrrole for CO2 capture from humid flue gases, Chem. Eng. J. 396 (2020) 125376, https://doi.org/10.1016/j.cej.2020.125376.

[35] M. Riyadh Atta, M. Shima Shaharun, Md. Maksudur Rahman Khan, B. Abdullah, A. Fadhl Al-Mahmodi, N. Diyan Mohd Ridzuan, T. Devi Munusamy, L. Jun Wei, Enhancing the photo-electrocatalytic properties of g-C3N4 by boron doping and ZIF-8 hybridization, Inorg. Chem. Commun. 148 (2023) 110235. https://doi.org/10.1016/j.inoche.2022.110235.

[36] N. Ishak, V. Jeyalakshmi, M. Setka, M. Grandcolas, B. Devadas, M. Šoóš, Upgrading of g-C3N4 semiconductor by a Nitrogen-doped carbon material: A photocatalytic degradation application, J. Environ. Chem. Eng. 11 (2023) 109381, https://doi.org/10.1016/j.jece.2023.109381.

[37] K. Žemlová, R. Mekkat, M. Šetka, M. Šoóš, Influence of PANI loading in hierarchically porous PANI/ZIF-8 composites on their sorption properties, (n.d.).

[38] S. Panneri, P. Ganguly, M. Mohan, B.N. Nair, A.A.P. Mohamed, K.G. Warrier, U. S. Hareesh, Photoregenerable, Bifunctional Granules of Carbon-Doped g-C $_3$ N $_4$ as Adsorptive Photocatalyst for the Efficient Removal of Tetracycline Antibiotic, ACS Sustain. Chem. Eng. 5 (2017) 1610–1618, https://doi.org/10.1021/acssuschemeng.6b02383.

[39] B. Zhu, P. Xia, W. Ho, J. Yu, Isoelectric point and adsorption activity of porous g-C3N4, Appl. Surf. Sci. 344 (2015) 188–195, https://doi.org/10.1016/j.apsusc.2015.03.086.

[40] S. Dong, Z. Zeng, W. Cai, Z. Zhou, C. Dou, H. Liu, J. Xia, The zeta potentials of g-C3N4 nanoparticles: Effect of electrolyte, ionic strength, pH, and humic acid, J. Nanoparticle Res. 21 (2019) 233, https://doi.org/10.1007/s11051-019-4686-z.

[41] L. Al-Gebory, M.P. Mengüç, The effect of pH on particle agglomeration and optical properties of nanoparticle suspensions, J. Quant. Spectrosc. Radiat. Transf. 219 (2018) 46–60, https://doi.org/10.1016/j.jqsrt.2018.07.020.

[42] L.-H. Kong, Y. Wu, R.-F. Shen, W.-J. Zhang, Z.-Y. Dong, W.-T. Ge, X.-J. Guo, X. Yan, Y. Chen, W.-Z. Lang, Combination of N-doped porous carbon and g-C3N4 for effective removal of organic pollutants via activated peroxymonosulfate, J. Environ. Chem. Eng. 10 (2022) 107808, https://doi.org/10.1016/j.jece.2022.107808.

[43] Q. Zhu, Y. Xuan, K. Zhang, K. Chang, Enhancing photocatalytic CO2 reduction performance of g-C3N4-based catalysts with non-noble plasmonic nanoparticles, Appl. Catal. B Environ. 297 (2021) 120440, https://doi.org/10.1016/j.apcatb.2021.120440.

[44] Q. Shen, C. Wu, Z. You, F. Huang, J. Sheng, F. Zhang, D. Cheng, H. Yang, g-C $_3$ N $_4$ nanoparticle@porous g-C $_3$ N $_4$ composite photocatalytic materials with significantly enhanced photo-generated carrier separation efficiency, J. Mater. Res. 35 (2020) 2148–2157, https://doi.org/10.1557/jmr.2020.182.

[45] Y. Wang, X. Bai, H. Qin, F. Wang, Y. Li, X. Li, S. Kang, Y. Zuo, L. Cui, Facile One-Step Synthesis of Hybrid Graphitic Carbon Nitride and Carbon Composites as High-Performance Catalysts for CO $_2$ Photocatalytic Conversion, ACS Appl. Mater. Interfaces 8 (2016) 17212–17219, https://doi.org/10.1021/acsami.6b03472.

[46] H. Wang, Z. Sun, Q. Li, Q. Tang, Z. Wu, Surprisingly advanced CO2 photocatalytic conversion over thiourea derived g-C3N4 with water vapor while introducing 200–420 nm UV light, J. CO2 Util. 14 (2016) 143–151, https://doi.org/10.1016/j.jcou.2016.04.006.

[47] J. Qiao, W. Ma, X. Du, X. Ma, Z. Liu, J. Li, G. Guan, A. Abudula, X. Hao, ZIF-8 derived carbon with confined sub-nanometer pores for electrochemically selective separation of chloride ions, Sep. Purif. Technol. 295 (2022) 121222, https://doi.org/10.1016/j.seppur.2022.121222.

[48] X. Chang, Y. Wang, X. Zhou, Y. Song, M. Zhang, ZIF-8-derived carbon-modified g-C $_3$ N $_4$ heterostructure with enhanced photocatalytic activity for dye degradation and hydrogen production, Dalton Trans. 50 (2021) 17618–17624, https://doi.org/10.1039/D1DT03385A.

[49] Y. Bao, K. Chen, AgCl/Ag/g-C3N4 Hybrid Composites: Preparation, Visible Light-Driven Photocatalytic Activity and Mechanism, Nano-Micro Lett. 8 (2016) 182–192, https://doi.org/10.1007/s40820-015-0076-y.

[50] Y. Gong, Z. Xu, J. Wu, J. Zhong, D. Ma, Enhanced photocatalytic hydrogen production performance of g-C3N4 with rich carbon vacancies, Appl. Surf. Sci. 657 (2024) 159790, https://doi.org/10.1016/j.apsusc.2024.159790.

[51] L. Xia, Z. Sun, Y. Wu, X.-F. Yu, J. Cheng, K. Zhang, S. Sarina, H.-Y. Zhu, H. Weerathunga, L. Zhang, J. Xia, J. Yu, X. Yang, Leveraging doping and defect

engineering to modulate exciton dissociation in graphitic carbon nitride for photocatalytic elimination of marine oil spill, Chem. Eng. J. 439 (2022) 135668, https://doi.org/10.1016/j.cej.2022.135668.
[52] D. Dvoranová, M. Mazúr, I. Papailias, T. Giannakopoulou, C. Trapalis, V. Brezová, EPR Investigations of G-C3N4/TiO2 Nanocomposites, Catalysts 8 (2018) 47, https://doi.org/10.3390/catal8020047.
[53] P. Wu, T. Zhou, Z. Tong, F. Xi, J. Lu, X. Li, W. Ma, S. Li, X. Yang, Balancing charge carrier density and exciton recombination in defective g-C3N4 for efficient photocatalytic hydrogen evolution, Prog. Nat. Sci. Mater. Int. 35 (2025) 238–244, https://doi.org/10.1016/j.pnsc.2024.12.015.
[54] Y. Li, W. Ho, K. Lv, B. Zhu, S.C. Lee, Carbon vacancy-induced enhancement of the visible light-driven photocatalytic oxidation of NO over g-C 3 N 4 nanosheets, Appl. Surf. Sci. 430 (2018) 380–389, https://doi.org/10.1016/j.apsusc.2017.06.054.
[55] C. Zhang, Q. Wan, H. Yu, J. Li, H. Zeng, H. Pang, W. Zhang, S. Liu, J. Huang, X. Li, Simultaneously manipulating excitons and charge carriers in g-C3N4 with abundant cyano groups and N vacancies for photocatalytic molecular oxygen activation, Sep. Purif. Technol. 361 (2025) 131291, https://doi.org/10.1016/j.seppur.2024.131291.
[56] H.-L. Chen, F.-Y. Liu, X. Xiao, J. Hu, B. Gao, D. Zou, C.-C. Chen, Visible-light-driven photocatalysis of carbon dioxide and organic pollutants by MFeO2 (M = Li, Na, or K), J. Colloid Interface Sci. 601 (2021) 758–772, https://doi.org/10.1016/j.jcis.2021.05.156.
[57] H.-L. Chen, F.-Y. Liu, Y.-Y. Lin, Z. Zuo, W.-T. Wu, Q. Qi, Z. Peng, D. Zou, C.-C. Chen, Photocatalytic CO2 reduction to C1–C5 hydrocarbons using K2Fe2O4/g-C3N4 as coupling photocatalyst, Mater. Today Sustain. 23 (2023) 100430, https://doi.org/10.1016/j.mtsust.2023.100430.
[58] H.-L. Chen, F.-Y. Liu, X. Xiao, Y.-Y. Lin, J. Hu, G.-Y. Liu, B. Gao, D. Zou, C.-C. Chen, Photoreduction of carbon dioxide and photodegradation of organic pollutants using alkali cobalt oxides MCoO2 (M = Li or Na) as catalysts, J. Environ. Manage. 313 (2022) 114930, https://doi.org/10.1016/j.jenvman.2022.114930.
[59] L. Wang, R.T. Yang, Significantly Increased CO $_2$ Adsorption Performance of Nanostructured Templated Carbon by Tuning Surface Area and Nitrogen Doping, J. Phys. Chem. C 116 (2012) 1099–1106, https://doi.org/10.1021/jp2100446.
[60] N. Bao, X. Hu, Q. Zhang, X. Miao, X. Jie, S. Zhou, Synthesis of porous carbon-doped g-C3N4 nanosheets with enhanced visible-light photocatalytic activity, Appl. Surf. Sci. 403 (2017) 682–690, https://doi.org/10.1016/j.apsusc.2017.01.256.
[61] X. Jiao, K. Zheng, Z. Hu, Y. Sun, Y. Xie, Broad-Spectral-Response Photocatalysts for CO $_2$ Reduction, ACS Cent. Sci. 6 (2020) 653–660, https://doi.org/10.1021/acscentsci.0c00325.
[62] L. Ge, C. Han, J. Liu, Y. Li, Enhanced visible light photocatalytic activity of novel polymeric g-C3N4 loaded with Ag nanoparticles, Appl. Catal. Gen. 409–410 (2011) 215–222, https://doi.org/10.1016/j.apcata.2011.10.006.
[63] J. Ran, H. Chen, S. Bi, Q. Guo, C. Yan, X. Tang, D. Cheng, G. Cai, X. Wang, Polydopamine-induced in-situ growth of zeolitic imidazolate framework-8/TiO2 nanoparticles on cotton fabrics for photocatalytic performance, Prog. Org. Coat. 152 (2021) 106123, https://doi.org/10.1016/j.porgcoat.2020.106123.
[64] R. Li, W. Li, C. Jin, Q. He, Y. Wang, Fabrication of ZIF-8@TiO2 micron composite via hydrothermal method with enhanced absorption and photocatalytic activities in tetracycline degradation, J. Alloys Compd. 825 (2020) 154008, https://doi.org/10.1016/j.jallcom.2020.154008.
[65] L. Ge, F. Zuo, J. Liu, Q. Ma, C. Wang, D. Sun, L. Bartels, P. Feng, Synthesis and Efficient Visible Light Photocatalytic Hydrogen Evolution of Polymeric g-C $_3$ N $_4$ Coupled with CdS Quantum Dots, J. Phys. Chem. C 116 (2012) 13708–13714, https://doi.org/10.1021/jp3041692.
[66] S. Cheng, Z. Sun, K.H. Lim, T.Z.H. Gani, T. Zhang, Y. Wang, H. Yin, K. Liu, H. Guo, T. Du, L. Liu, G.K. Li, Z. Yin, S. Kawi, Emerging Strategies for CO $_2$ Photoreduction to CH $_4$: From Experimental to Data-Driven Design, Adv. Energy Mater. 12 (2022) 2200389, https://doi.org/10.1002/aenm.202200389.
[67] H. Ou, G. Li, W. Ren, B. Pan, G. Luo, Z. Hu, D. Wang, Y. Li, Atomically Dispersed Au-Assisted C–C Coupling on Red Phosphorus for CO $_2$ Photoreduction to C $_2$ H $_6$, J. Am. Chem. Soc. 144 (2022) 22075–22082, https://doi.org/10.1021/jacs.2c09424.
[68] R. Akbarzadeh, C.S.L. Fung, R.A. Rather, I.M.C. Lo, One-pot hydrothermal synthesis of g-C3N4/Ag/AgCl/BiVO4 micro-flower composite for the visible light degradation of ibuprofen, Chem. Eng. J. 341 (2018) 248–261, https://doi.org/10.1016/j.cej.2018.02.042.
[69] Z. Qu, P. Liu, X. Yang, F. Wang, W. Zhang, C. Fei, Microstructure and Characteristic of BiVO4 Prepared under Different pH Values: Photocatalytic Efficiency and Antibacterial Activity, Materials 9 (2016) 129, https://doi.org/10.3390/ma9030129.
[70] J. Pei, H. Li, S. Zhuang, D. Zhang, D. Yu, Recent Advances in g-C3N4 Photocatalysts: A Review of Reaction Parameters, Structure Design and Exfoliation Methods, Catalysts 13 (2023) 1402, https://doi.org/10.3390/catal13111402.
[71] J. Dong, Y. Zhang, M.I. Hussain, W. Zhou, Y. Chen, L.-N. Wang, g-C3N4: Properties, Pore Modifications, and Photocatalytic Applications, Nanomaterials 12 (2021) 121, https://doi.org/10.3390/nano12010121.
[72] Z. Lu, D. Zeng, H. Zheng, Q. Liu, X. Gao, X. He, L. Wei, W.-J. Ong, Enhanced interfacial electron transfer and boosted visible-light photocatalytic hydrogen evolution activity of g-C3N4 by noble-metal-free MoSe2 nanoparticles, J. Mater. Sci. 55 (2020) 13114–13126, https://doi.org/10.1007/s10853-020-04945-4.
[73] R. Zhao, X. Sun, Y. Jin, J. Han, L. Wang, F. Liu, Au/Pd/g-C3N4 nanocomposites for photocatalytic degradation of tetracycline hydrochloride, J. Mater. Sci. 54 (2019) 5445–5456, https://doi.org/10.1007/s10853-018-03278-7.
[74] N. Ding, L. Zhang, M. Hashimoto, K. Iwasaki, N. Chikamori, K. Nakata, Y. Xu, J. Shi, H. Wu, Y. Luo, D. Li, A. Fujishima, Q. Meng, Enhanced photocatalytic activity of mesoporous carbon/C3N4 composite photocatalysts, J. Colloid Interface Sci. 512 (2018) 474–479, https://doi.org/10.1016/j.jcis.2017.10.081.